

Metal-insulator transition in transition metal dichalcogenide heterobilayer: accurate treatment of interaction

Yubo Yang,¹ Miguel Morales,¹ and Shiwei Zhang¹

¹Center for Computational Quantum Physics, Flatiron Institute, New York, NY, 10010, USA

(Dated: January 19, 2024)

Transition metal dichalcogenide superlattices provide an exciting new platform for exploring and understanding a variety of phases of matter. The moiré continuum Hamiltonian, of two-dimensional jellium in a modulating potential, provides a fundamental model for such systems. Accurate computations with this model are essential for interpreting experimental observations and making predictions for future explorations. In this work, we combine two complementary quantum Monte Carlo (QMC) methods, phaseless auxiliary field quantum Monte Carlo and fixed-phase diffusion Monte Carlo, to study the ground state of this Hamiltonian. We observe a metal-insulator transition between a paramagnetic and a 120° Néel ordered state as the moiré potential depth and the interaction strength are varied. We find significant differences from existing results by Hartree-Fock and exact diagonalization studies. In addition, we benchmark density-functional theory, and suggest an optimal hybrid functional which best approximates our QMC results.

Introduction — Correlated insulators^{1–6} and other interaction-driven electronic states^{7–10} have been realized in moiré superstructures created by the interference between two slightly mismatched 2D crystals¹¹. Multi-layer transition metal dichalcogenide (TMDC) systems have become one of the focal points of recent experimental^{10,12} and theoretical^{13,14} pursuits. The low-energy quasiparticles in these semiconductor interfaces traverse a smooth potential energy landscape with moiré periodicity, because the band edge energy changes with the local geometry and interlayer coupling^{15,16}, which vary on the moiré scale. The long moiré wavelength allows their physics to be largely separated from atomistic details¹⁷. This creates the opportunity to realize tunable systems whose characteristic density variations are on the moiré scale. The strong electron-electron interactions coupled with band engineering and other effects have allowed a fascinating array of quantum phases to be realized.

The moiré continuum Hamiltonian (MCH)^{18,19}, of two-dimensional electron gas (2DEG) in a periodic external moiré potential, is a fundamental model for such systems. The MCH is directly connected to experiments. The external moiré potential can be obtained by measuring the band edge variation in a scanning tunneling microscopy (STM) experiment^{5,16}, while the quasiparticle dispersion can be measured in angle-resolved photoemission spectroscopy (ARPES) experiments²⁰. Further, it contains realistic long-range Coulomb interaction between the electrons. The MCH is also directly connected to *ab initio* calculations. It can be derived from a large-scale atomistic density functional theory (DFT) calculation^{18,21–24} by matching the band structure near the Fermi level.

Computing the properties of the MCH can provide insight into the physics in 2D materials — a rich collection has already observed in experiments and undoubtedly much remains to be realized. In addition, the ability to perform accurate computations for the MCH will allow us to make reliable predictions. Seemingly simple mod-

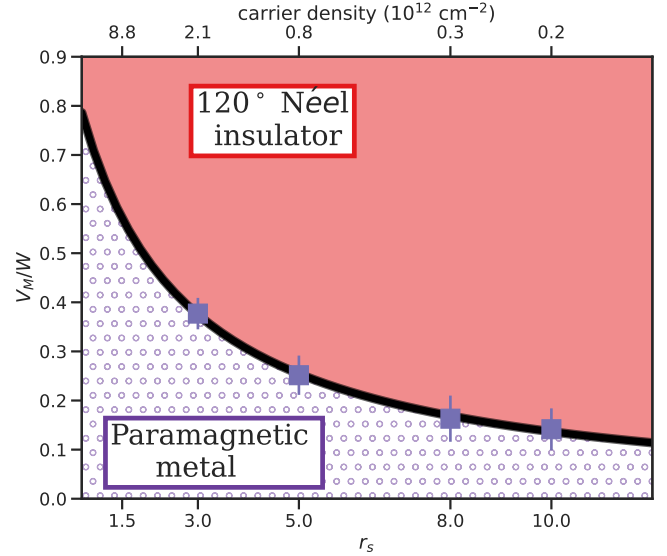


FIG. 1. Phase diagram of the moiré continuum model at half filling. V_M/W gives the strength of the moiré potential, while r_s , the Wigner-Seitz density parameter, is a measure of the interaction strength. The ground state is a paramagnetic metal at high density or in a shallow moiré potential, and transitions into a 120° Néel magnetic insulator with decreasing density or increasing potential. The solid black line identifies a MIT boundary. Error bars indicate the estimated systematic uncertainty of the MIT. The top label maps r_s to hole density in hBN-encapsulated $WSe_2/MoSe_2$.

els, such as the uniform electron gas and the Hubbard model, have provided enormous value in improving our ability to understand and compute much more realistic and complex materials. The MCH shares this simplicity, and has strong connections to both of these models. In the deep-moiré limit, it downfolds to the Hubbard model on triangular and related lattices^{25–27}. Although non-local interactions are expected to be important^{28–30}. In the absence of moiré, the MCH reduces to the 2DEG,

which has long served as a valuable model for semiconductor interfaces^{31,32}. The inclusion of the moiré potential allows a simple and yet rather realistic modeling of the environment in 2D TMDC materials.

Much remains to be understood about the properties of the MCH, and little is available in terms of accurate quantitative information. In this paper, we use two complementary many-body QMC methods to explore interesting regimes of the MCH, which involve strong interaction and its delicate interplay with correlation. No existing theoretical or computational results can capture these intricacies with enough reliability to predict the correlated phases in the model, which requires accurate treatment of both exchange and correlation effects. We find a first-order metal-insulator transition (MIT) between a paramagnetic metal and a 120° Néel insulator.

Model — The MCH, which can be thought of as an effective model for holes in the valence band at the interface of TMDC systems, takes the form

$$H = -\frac{\hbar^2}{2|m^*|} \sum_i \nabla_i^2 - V_M \sum_i \Lambda(\mathbf{r}_i) + \frac{e^2}{4\pi\epsilon} \sum_{i<j} \frac{1}{|\mathbf{r}_i - \mathbf{r}_j|}, \quad (1)$$

where $m^* < 0$ is the hole effective mass and ϵ is the permittivity of the dielectric environment. The parameters V_M and ϕ define the depth and shape of the moiré potential. We take $\Lambda(\mathbf{r}) = \sum_{j=1}^3 2 \cos(\mathbf{r} \cdot \mathbf{g}_j + \phi)$, where \mathbf{g}_j are three of the smallest non-zero reciprocal lattice vectors of the moiré unit cell.

Given a filling factor ν , the moiré lattice constant a_M defines the Wigner-Seitz radius a , which sets the kinetic and interaction energy scales, $W \equiv \frac{\hbar^2}{|m^*|a^2}$ and $U \equiv \frac{e^2}{4\pi\epsilon a}$.

Defining an effective $a_B^* \equiv \frac{\hbar^2}{|m^*|} / \frac{e^2}{4\pi\epsilon}$ as length unit, we can express a in reduced units: $r_s \equiv a/a_B^* = U/W$. Using W as energy unit, the MCH in eq. (1) reduces to

$$\mathcal{H} = -\frac{1}{2} \sum_i \tilde{\nabla}_i^2 - \lambda \sum_i \tilde{\Lambda}(\tilde{\mathbf{r}}_i) + r_s \sum_{i<j} \frac{1}{|\tilde{\mathbf{r}}_i - \tilde{\mathbf{r}}_j|}, \quad (2)$$

where all lengths are scaled by a : $\tilde{\mathbf{r}} \equiv \mathbf{r}/a$, $\tilde{\mathbf{g}} \equiv \mathbf{g}a$ ($\tilde{\Lambda}$ contains $\tilde{\mathbf{g}}$). The two parameters, $\lambda \equiv V_M/W$ and r_s , fully specify the system. To connect with experiments, m^* and ϵ are needed.

We consider $m^* = -0.35$, $\epsilon/\epsilon_0 = 4.5$, $\phi = 26^\circ$, and half filling $\nu = 1$ as inspired by studies of hexagonal boron nitride (hBN)-encapsulated $\text{WSe}_2/\text{MoSe}_2$ ^{5,22,25,27,33}. Given these choices, $a_M = 10$ nm corresponds to $r_s = 7.7$.

The actual experimental setup is more complicated than the MCH^{34–36} of eq. (1). Atomic reconstruction^{37–39}, gate screening^{40,41}, and disorder^{42–44} all have the potential to make the physics of the device qualitatively different. However, the MCH Hamiltonian captures essential features which drive much of the interesting physics in 2D TMDC materials. The interaction terms in the MCH can be modified to bring the model

closer to experiment. Further, the addition of a spin-orbit term can facilitate the modeling of Janus TMDC bilayers⁴⁵.

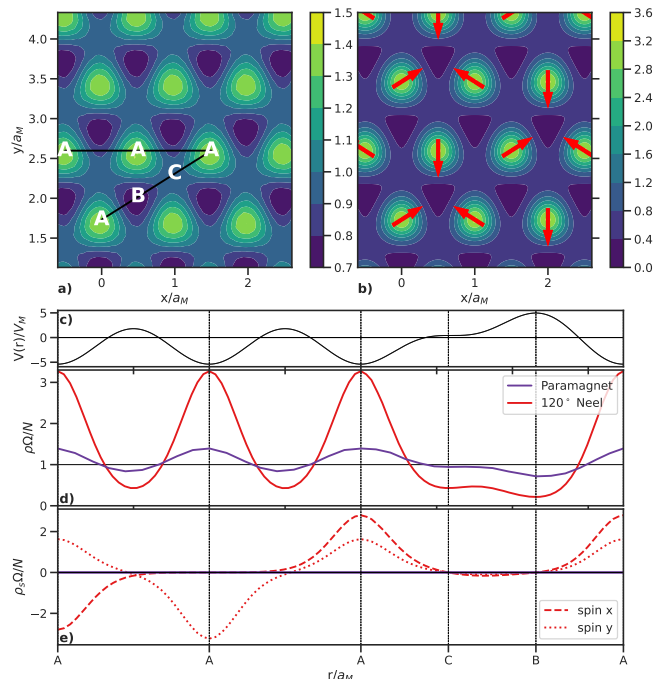


FIG. 2. Spin and charge densities of representative **a)** metal and **b)** insulator phases (at $r_s = 3$ and with $V_M/W = 0.2$ and 0.6 , respectively). The linecuts are drawn for the path shown as a black line in **a)**. Panel **c)** shows the moiré potential, while **d)** and **e)** show the charge and spin (in 120° Néel phase only) densities, respectively.

Methods — We apply two QMC methods, diffusion Monte Carlo (DMC)⁴⁶ and auxiliary field quantum Monte Carlo (AFQMC)^{47–49} to study the ground state of the MCH in Eq. (2). They are among the most accurate many-body methods for strongly correlated systems^{50–53}. One of the major challenges in reliably characterizing the properties of a system such as the MCH is to maintain accuracy in realistic hamiltonians, which contain long-range Coulomb interactions, and still approach the thermodynamic limit. The QMC methods we employ allow us to achieve these objectives.

We use the non-collinear spin implementation^{54–57} of fixed-phase DMC (FP-DMC)⁵⁸, and the GPU-accelerated phaseless-AFQMC (ph-AFQMC)^{47,59,60}. FP-DMC is variational and works directly in the complete-basis-set limit. We use it to locate the MIT boundary by comparing the total energies of metallic and insulating states. Properties including the spin and charge densities and momentum distributions are computed by AFQMC using the mixed estimator⁶¹. They are cross-checked with DMC calculations where possible, with consistent results between the two methods. See Supplemental Material [url] for details, which include Ref.⁷⁷.

Effective single-particle theories such as Hartree-Fock (HF) and DFT replace the many-body interaction term with an effective single-particle potential. In this work, we also benchmark their reliability against our QMC results. One goal of this effort is to identify the best independent-particle approach for 2D TMDC systems, which will greatly help initial screening of basic properties using relatively inexpensive and quick computations to support the fast-growing experimental effort. It is important to emphasize that these benchmarks are only a first step, however, since the performance will vary as we vary the system parameters (including, among others, ν and ϕ). We perform DFT calculations via the local density approximation (LDA)⁶² as well as hybrid functionals⁶³.

Our QMC calculations are typically performed in 36- and 144-electron systems with 4×4 and 2×2 twist-averaged boundary condition, respectively. Structure factor based finite-size correction^{64–66} and grand-canonical twists⁶⁷ are used to obtain the momentum distribution in the metallic phase. All DMC calculations use a fictitious spin mass of 500 a.u. to sample spins. In FP-DMC, we use a Slater-Jastrow wavefunction ansatz, which is optimized with variational Monte Carlo. The Jastrow contains short-range two-body correlations, represented by B-splines. Our ph-AFQMC calculations are performed using a Kohn-Sham orbital basis. We use single Slater determinant trial wavefunctions generated using either HF or LDA. The lowest-energy trial is used to calculate QMC properties. In the paramagnetic metal phase, the LDA trial is chosen, otherwise the insulating HF trial has lower energy. The QMC calculations are carried out using QMCPACK 3.15.9^{68,69} with appropriate 2D modifications. We perform HF and DFT calculations using quantum espresso (QE) 7.1^{70,71}, modified to perform 2D calculations. We use the 2D LDA functional from libxc 5.1.7^{72,73}, which is based on DMC data obtained by C. Attacalite *et al.*⁷⁴.

Results and Discussions — Figure 1 shows the results of our QMC phase diagram of the MCH. As the electron-electron interaction, U , and the external moiré potential, V_M , are increased from zero, the system undergoes a first-order transition from a paramagnetic metal to a 120° Néel insulator. The strength of the moiré potential λ required to induce the transition decreases monotonically with increasing r_s .

The limiting behaviors of the MCH phase diagram are independent of model details. At constant V_M and in the high-density limit ($r_s \rightarrow 0$), we expect a paramagnetic metal because the kinetic energy dominates. At $V_M = 0$, the MCH reduces to the 2DEG, thus we expect a transition from the paramagnetic metal to a Wigner crystal (WC) at $r_s = 31 \pm 1$ ⁷⁵. While not explored in this work, we anticipate important changes in the charge and spin properties in the vicinity of the transition as r_s increases towards the WC limit. For example, magnetic interactions become nearly degenerate in the low-density limit, opening the possibilities for exotic spin states⁷⁶. While

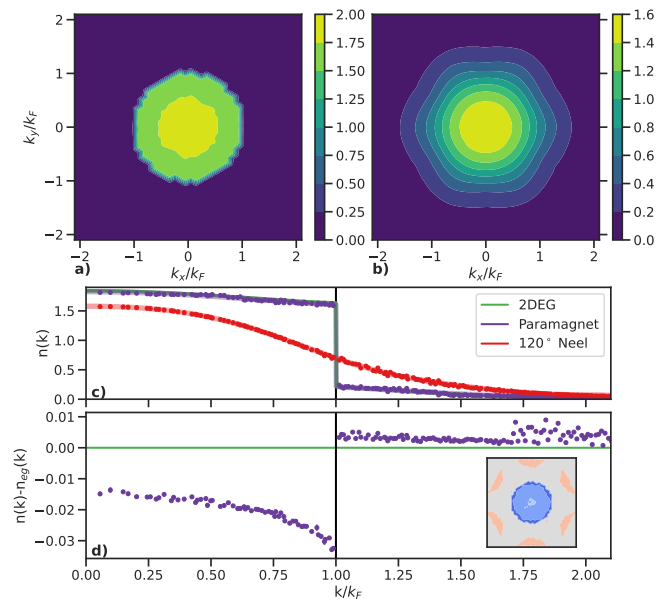


FIG. 3. Momentum distribution of the same representative systems as in Fig. 2. Panels **a)** and **b)** show $n(\mathbf{k})$ for the metallic and insulating phases, respectively. Panel **c)** plots $n(|\mathbf{k}|)$ for both systems, along with that of the 2DEG for reference. The metallic system is barely discernible from the 2DEG, both with a discontinuity at $k = k_F$. Panel **d)** shows the difference between them with a magnified view. Secondary Fermi surfaces are present in the metallic phase, as seen in the inset.

the WC is translationally invariant, any finite V_M pins the WC, allowing its density correlations to be visualized in single-particle densities.

In Fig. 2, we quantify the spin and charge densities of the metallic and insulating phases. Density is normalized such that $\int_{\Omega} \rho(\mathbf{r}) d^2\mathbf{r} = N$. Both phases show charge accumulation at the moiré minima (A sites) and depletion at the maxima (B sites), whereas only the insulating phase shows significant charge depletion at the saddle points (C sites). The paramagnetic metal has nearly uniform charge density, with moderate charge accumulation and depletion, peak-to-trough ratio ~ 2 , which mirror the moiré potential. In contrast, this ratio is > 15 in the 120° Néel phase, where there is little charge at the maxima of the moiré potential (B sites). Site-integrated spin densities, shown as red arrows in the top right panel of Fig. 2, realize the 120° Néel magnetic order. The charge densities have C_{3z} symmetry due to the internal structure of the moiré potential at $\phi = 26^\circ$, which makes the B and C sites different. They become equivalent when $\phi = 60^\circ$, which could be realized in honeycomb moiré materials¹⁹.

We also compute the electronic momentum distributions, which are shown in Fig. 3. The paramagnetic metal phase has nearly identical momentum distribution to the 2DEG despite the significant amount of external moiré potential ($V_M/W = 0.2$) imposed upon it. The Fermi

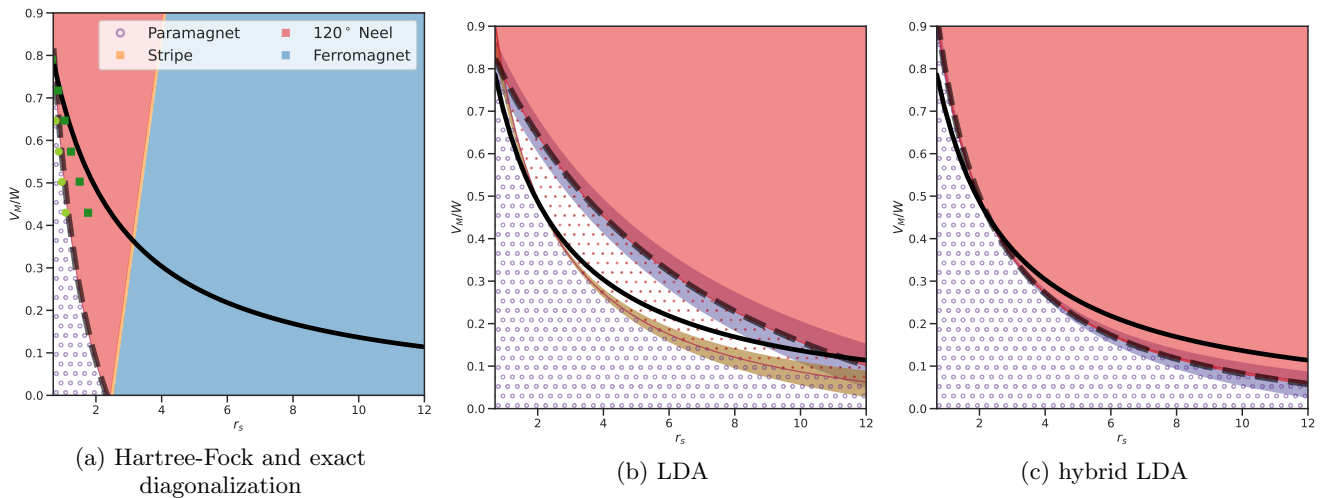


FIG. 4. Qualitatively different phase diagrams created by various approximations of correlation effects. Predictions from three independent-particle theories and exact diagonalization of small systems are benchmarked by the result in Fig. 1, with the black solid line marking the MIT phase boundary from QMC. The dashed line marks the MIT from each independent-particle theory. **(a)** HF predicts an early MIT, which is restricted to high density ($r_s < 2.5$), and favors a ferromagnetic state as interaction increases. A small region of collinear stripe phase sits between the noncollinear and ferromagnetic phases. HF results for the MIT from the present study and from Ref.²⁷ (light green dots) are in good agreement. Exact diagonalization predictions for the MIT from Ref.³³ are also shown (dark green dots), which exhibits growing error at larger r_s . **(b)** LDA favors the metallic state, thus a late MIT in deep moiré potential. It predicts a bandgap closure within the magnetic phase, resulting in a metallic spin density wave (SDW) phase that retains the long-range magnetic order (red dot-hatched region). The shaded areas around the DFT transition lines are uncertainty estimates due to convergence errors. **(c)** Hybrid LDA with 50% exact exchange is able to yield a phase diagram in this system which is in qualitative agreement with QMC.

surface remains isotropic at $k_F = \sqrt{2}/r_s$ while the moiré potential and electron interaction scatter a small amount of momentum density from inside the Fermi surface to the high-momentum tail. The secondary Fermi surfaces, too faint to be visible in the main contour plot, are noticeable in the linecut around $1.75k_F$ and in the difference contour in the inset. The 120° Néel insulator has a smooth momentum distribution with no sign of discontinuity.

Accurate treatment of interaction and correlation is crucial in determining the phase diagram of the MCH. Our QMC phase diagram (Fig. 1) is a major revision of that from HF (Fig. 4(a)), where correlation effects are ignored. A previous exact diagonalization (ED) study³³ found a continuous/weakly first-order MIT, which lies between the HF and QMC predictions. The small system and basis sizes used in the ED study lead to an underestimation of the gap. The 120° phase has an indirect band gap, so a continuous metal-insulator transition is possible in principle. However, we find a first-order transition in our most accurate calculations within the finite resolution of our scan of the two parameters λ and r_s . See Supplemental Material [url]. As shown in Fig. 4(b), LDA predicts an early gap closure in the magnetic state, leading to a spin density wave (SDW) phase between the metal and the 120° Néel insulator. However, by introducing exact exchange interaction from HF into LDA via a hybrid functional, the charge gap increases to eliminate the SDW phase, making the hybrid LDA phase diagram in qualitative agreement with QMC as shown in Fig. 4(c).

The magnetization disappears abruptly across the transition boundary, driving the charge gap to zero discontinuously. This hybrid functional can thus potentially serve as an inexpensive tool for quick first theoretical explorations in these systems, although it is important to keep in mind its empirical nature, especially in predicting properties.

All our calculations are at $T = 0K$. To better connect with experiments, we estimate the exchange energy scale by computing the energy cost, ΔE , to flip a spin in the AFM “stripe” phase, which contains alternating stripes of up and down spins. In a nearest-neighbor Heisenberg model $H = \sum_{\langle i,j \rangle} JS_i S_j$, $\Delta E = 4J$. At $r_s = 8$ and $\lambda = 1$, we obtain $J \approx 40$ mK, which is seen to decrease rapidly with increasing λ . See Supplemental Material [url] for details. This is consistent with our total energy comparisons which indicate that the “stripe” phase is nearly degenerate with the 120° phase. The near-degeneracy of magnetic states can lead to exotic spin physics, which we hope to explore in future work.

Conclusion and Outlook — We have characterized the ground-state properties of the MCH at half-filling in the intermediate to high density regime. This model captures key ingredients in TMDC systems, namely the presence of the moiré potential and strong correlation physics of the two-dimensional electron gas, and can serve as a fundamental model for providing quantitative understanding of these fascinating systems. Combining two different QMC methods, we obtain benchmark-quality data on the

energetics, momentum distributions, and the strengths of the magnetic and charge ordering. The system transitions from a paramagnetic metal to a 120° Néel insulator phase as the moiré is deepened or as the density is lowered. Existing approximate treatments, either via independent-electron approaches or by simplified lattice models, were seen to result in significant discrepancies in the predicted properties. We tested 2D LDA and hybrid functionals and found that a hybrid mix of 50% yields a reasonable ground-state phase diagram in this system when compared to our QMC predictions.

We hope that this study paves the way for QMC and

other many-body studies of the MCH and related systems. Many questions remain to be explored, including the physics — and potentially more interesting/exotic phases — at lower density, with other filling fractions, other structures (moiré patterns), the effect of spin-orbit coupling and valley degrees of freedom.

Acknowledgment — We thank the Flatiron Institute Scientific Computing Center for computational resources and technical support. The Flatiron Institute is a division of the Simons Foundation. We thank Andrew Millis, Cody Melton, David Ceperley, Daniele Guerci, Jiawei Zang, Liang Fu, and Scott Jensen for useful discussions.

-
- ¹ Y. Tang, L. Li, T. Li, Y. Xu, S. Liu, K. Barmak, K. Watanabe, T. Taniguchi, A. H. MacDonald, J. Shan, and K. F. Mak, *Nature* **579**, 353 (2020), 1910.08673.
- ² Y. Xu, S. Liu, D. A. Rhodes, K. Watanabe, T. Taniguchi, J. Hone, V. Elser, K. F. Mak, and J. Shan, *Nature* **587**, 214 (2020), 2007.11155.
- ³ E. C. Regan, D. Wang, C. Jin, M. I. Bakti Utama, B. Gao, X. Wei, S. Zhao, W. Zhao, Z. Zhang, K. Yumigeta, M. Blei, J. D. Carlström, K. Watanabe, T. Taniguchi, S. Tongay, M. Crommie, A. Zettl, and F. Wang, *Nature* **579**, 359 (2020).
- ⁴ L. Wang, E.-M. Shih, A. Ghiotto, L. Xian, D. A. Rhodes, C. Tan, M. Claassen, D. M. Kennes, Y. Bai, B. Kim, K. Watanabe, T. Taniguchi, X. Zhu, J. Hone, A. Rubio, A. N. Pasupathy, and C. R. Dean, *Nature Materials* **19**, 861 (2020).
- ⁵ S. Shabani, D. Halbertal, W. Wu, M. Chen, S. Liu, J. Hone, W. Yao, D. N. Basov, X. Zhu, and A. N. Pasupathy, *Nature Physics* **17**, 720 (2021), 2008.07696.
- ⁶ X. Huang, T. Wang, S. Miao, C. Wang, Z. Li, Z. Lian, T. Taniguchi, K. Watanabe, S. Okamoto, D. Xiao, S.-F. Shi, and Y.-T. Cui, *Nature Physics* **17**, 715 (2021), 2007.11155.
- ⁷ C. Jin, Z. Tao, T. Li, Y. Xu, Y. Tang, J. Zhu, S. Liu, K. Watanabe, T. Taniguchi, J. C. Hone, L. Fu, J. Shan, and K. F. Mak, *Nature Materials* **20**, 940 (2021), 2007.12068.
- ⁸ X. Wang, C. Xiao, H. Park, J. Zhu, C. Wang, T. Taniguchi, K. Watanabe, J. Yan, D. Xiao, D. R. Gamelin, W. Yao, and X. Xu, *Nature* **604**, 468 (2022), 2203.07161.
- ⁹ Z. Tao, B. Shen, S. Jiang, T. Li, L. Li, L. Ma, W. Zhao, J. Hu, K. Pistunova, K. Watanabe, T. Taniguchi, T. F. Heinz, K. F. Mak, and J. Shan, arXiv e-prints , arXiv:2208.07452 (2022), 2208.07452 [cond-mat.mes-hall].
- ¹⁰ W. Zhao, B. Shen, Z. Tao, Z. Han, K. Kang, K. Watanabe, T. Taniguchi, K. F. Mak, and J. Shan, arXiv e-prints , arXiv:2211.00263 (2022), 2211.00263 [cond-mat.str-el].
- ¹¹ K. F. Mak and J. Shan, *Nature Nanotechnology* **17**, 686 (2022).
- ¹² B. A. Foutty, J. Yu, T. Devakul, C. R. Kometter, Y. Zhang, K. Watanabe, T. Taniguchi, L. Fu, and B. E. Feldman, arXiv e-prints , arXiv:2206.10631 (2022), 2206.10631 [cond-mat.mes-hall].
- ¹³ M. Davydova, Y. Zhang, and L. Fu, arXiv e-prints , arXiv:2206.01221 (2022), 2206.01221 [cond-mat.str-el].
- ¹⁴ D. Guerci, J. Wang, J. Zang, J. Cano, J. H. Pixley, and A. Millis, arXiv e-prints , arXiv:2207.06476 (2022), 2207.06476 [cond-mat.str-el].
- ¹⁵ H. Li, S. Li, M. H. Naik, J. Xie, X. Li, J. Wang, E. Regan, D. Wang, W. Zhao, S. Zhao, S. Kahn, K. Yumigeta, M. Blei, T. Taniguchi, K. Watanabe, S. Tongay, A. Zettl, S. G. Louie, F. Wang, and M. F. Crommie, *Nature Materials* **20**, 945 (2021).
- ¹⁶ R. Nieken, A. Roche, F. Mahdikhanyarvejahany, T. Taniguchi, K. Watanabe, M. R. Koehler, D. G. Mandrus, J. Schaibley, and B. J. LeRoy, *APL Materials* **10** (2022), 10.1063/5.0084358, 031107.
- ¹⁷ B. Padhi, R. Chitra, and P. W. Phillips, *Physical Review B* **103**, 125146 (2021), 2009.13536.
- ¹⁸ F. Wu, T. Lovorn, and A. H. MacDonald, *Physical Review B* **97**, 035306 (2018), 1710.10278.
- ¹⁹ M. Angeli and A. H. MacDonald, *Proceedings of the National Academy of Sciences* **118**, 1 (2021).
- ²⁰ N. R. Wilson, P. V. Nguyen, K. Seyler, P. Rivera, A. J. Marsden, Z. P. L. Laker, G. C. Constantinescu, V. Kandyba, A. Barinov, N. D. M. Hine, X. Xu, and D. H. Cobden, *Science Advances* **3**, e1601832 (2017), <https://www.science.org/doi/pdf/10.1126/sciadv.1601832>.
- ²¹ J. Jung, A. Raoux, Z. Qiao, and A. H. MacDonald, *Phys. Rev. B* **89**, 205414 (2014).
- ²² Y. Zhang, N. F. Q. Yuan, and L. Fu, *Physical Review B* **102**, 201115(R) (2020), 1910.14061.
- ²³ S. Carr, S. Fang, and E. Kaxiras, *Nature Reviews Materials* **5**, 748 (2020).
- ²⁴ L. Xian, M. Claassen, D. Kiese, M. M. Scherer, S. Trebst, D. M. Kennes, and A. Rubio, *Nature Communications* **12**, 5644 (2021), 2004.02964.
- ²⁵ F. Wu, T. Lovorn, E. Tutuc, and A. H. MacDonald, *Physical Review Letters* **121**, 026402 (2018).
- ²⁶ H. Pan, F. Wu, and S. Das Sarma, *Physical Review Research* **2**, 033087 (2020), 2004.04168.
- ²⁷ N. C. Hu and A. H. MacDonald, *Physical Review B* **104**, 214403 (2021), 2108.02159.
- ²⁸ N. Morales-Durán, N. C. Hu, P. Potasz, and A. H. MacDonald, *Phys. Rev. Lett.* **128**, 217202 (2022).
- ²⁹ Y. Zhou, D. N. Sheng, and E.-A. Kim, *Phys. Rev. Lett.* **128**, 157602 (2022).
- ³⁰ N. Gneist, L. Classen, and M. M. Scherer, *Phys. Rev. B* **106**, 125141 (2022).
- ³¹ T. Ando, A. B. Fowler, and F. Stern, *Rev. Mod. Phys.* **54**, 437 (1982).
- ³² A. V. Chaplik, *JETP* **35**, 395 (1972).

- ³³ N. Morales-Durán, A. H. MacDonald, and P. Potasz, *Physical Review B* **103**, L241110 (2021), 2011.13558.
- ³⁴ T. Li, S. Jiang, L. Li, Y. Zhang, K. Kang, J. Zhu, K. Watanabe, T. Taniguchi, D. Chowdhury, L. Fu, J. Shan, and K. F. Mak, *Nature* **597**, 350 (2021), 2103.09779.
- ³⁵ A. Ghiotto, E.-M. Shih, G. S. S. G. Pereira, D. A. Rhodes, B. Kim, J. Zang, A. J. Millis, K. Watanabe, T. Taniguchi, J. C. Hone, L. Wang, C. R. Dean, and A. N. Pasupathy, *Nature* **597**, 345 (2021), 2103.09796.
- ³⁶ Y. Tang, J. Gu, S. Liu, K. Watanabe, T. Taniguchi, J. C. Hone, K. F. Mak, and J. Shan, *Nature Communications* **13**, 4271 (2022).
- ³⁷ H. Yoo, R. Engelke, S. Carr, S. Fang, K. Zhang, P. Cazeaux, S. H. Sung, R. Hovden, A. W. Tsen, T. Taniguchi, K. Watanabe, G.-C. Yi, M. Kim, M. Lusk, E. B. Tadmor, E. Kaxiras, and P. Kim, *Nature Materials* **18**, 448 (2019), 1804.03806.
- ³⁸ D. Halbertal, N. R. Finney, S. S. Sunku, A. Kerelsky, C. Rubio-Verdú, S. Shabani, L. Xian, S. Carr, S. Chen, C. Zhang, L. Wang, D. Gonzalez-Acevedo, A. S. McLeod, D. Rhodes, K. Watanabe, T. Taniguchi, E. Kaxiras, C. R. Dean, J. C. Hone, A. N. Pasupathy, D. M. Kennes, A. Rubio, and D. N. Basov, *Nature Communications* **12**, 1 (2021), 2008.04835.
- ³⁹ Z. Li, F. Tabataba-Vakili, S. Zhao, A. Rupp, I. Bilgin, Z. Herdegen, B. März, K. Watanabe, T. Taniguchi, G. R. Schleder, A. S. Baimuratov, E. Kaxiras, K. Müller-Caspary, and A. Högele, “Lattice reconstruction in $m\text{-}2\text{-}w\text{-}se_2$ heterobilayers synthesized by chemical vapor deposition,” (2022), 2212.07686 [cond-mat.mes-hall].
- ⁴⁰ B. Spivak and S. A. Kivelson, *Phys. Rev. B* **70**, 155114 (2004).
- ⁴¹ Y. Tang, K. Su, L. Li, Y. Xu, S. Liu, K. Watanabe, T. Taniguchi, J. Hone, C. M. Jian, C. Xu, K. F. Mak, and J. Shan, *Nature Nanotechnology* (2023), 10.1038/s41565-022-01309-8.
- ⁴² Y. Tan, P. K. H. Tsang, and V. Dobrosavljević, *Nature Communications* **13**, 7469 (2022), 2112.11522.
- ⁴³ S. Ahn and S. Das Sarma, *Physical Review B* **105**, 115114 (2022).
- ⁴⁴ S. Kim, T. Senthil, and D. Chowdhury, *Physical Review Letters* **130**, 066301 (2023), 2204.10865.
- ⁴⁵ M. Angeli, G. R. Schleder, and E. Kaxiras, *Phys. Rev. B* **106**, 235159 (2022).
- ⁴⁶ W. M. C. Foulkes, L. Mitás, R. J. Needs, and G. Rajagopal, *Rev. Mod. Phys.* **73**, 33 (2001).
- ⁴⁷ S. Zhang and H. Krakauer, *Physical Review Letters* **90**, 136401 (2003), 0208340 [cond-mat].
- ⁴⁸ S. Zhang, “Auxiliary-field quantum monte carlo for correlated electron systems,” in *Emergent Phenomena in Correlated Matter*, Vol. 3 (Forschungszentrum Jülich GmbH, 2013) Chap. 15.
- ⁴⁹ H. Shi and S. Zhang, *The Journal of Chemical Physics* **154** (2021), 10.1063/5.0031024, 024107, https://pubs.aip.org/aip/jcp/article-pdf/doi/10.1063/5.0031024/15584016/024107_1.online.pdf.
- ⁵⁰ J. P. F. LeBlanc, A. E. Antipov, F. Becca, I. W. Bulik, G. K.-L. Chan, C.-M. Chung, Y. Deng, M. Ferrero, T. M. Henderson, C. A. Jiménez-Hoyos, E. Kozik, X.-W. Liu, A. J. Millis, N. V. Prokof'ev, M. Qin, G. E. Scuseria, H. Shi, B. V. Svistunov, L. F. Tocchio, I. S. Tupitsyn, S. R. White, S. Zhang, B.-X. Zheng, Z. Zhu, and E. Gull (Simons Collaboration on the Many-Electron Problem), *Phys. Rev. X* **5**, 041041 (2015).
- ⁵¹ M. Motta, D. M. Ceperley, G. K.-L. Chan, J. A. Gomez, E. Gull, S. Guo, C. A. Jiménez-Hoyos, T. N. Lan, J. Li, F. Ma, A. J. Millis, N. V. Prokof'ev, U. Ray, G. E. Scuseria, S. Sorella, E. M. Stoudenmire, Q. Sun, I. S. Tupitsyn, S. R. White, D. Zgid, and S. Zhang (Simons Collaboration on the Many-Electron Problem), *Phys. Rev. X* **7**, 031059 (2017).
- ⁵² M. Motta, C. Genovese, F. Ma, Z.-H. Cui, R. Sawaya, G. K.-L. Chan, N. Chepiga, P. Helms, C. Jiménez-Hoyos, A. J. Millis, U. Ray, E. Ronca, H. Shi, S. Sorella, E. M. Stoudenmire, S. R. White, and S. Zhang (Simons Collaboration on the Many-Electron Problem), *Phys. Rev. X* **10**, 031058 (2020).
- ⁵³ K. T. Williams, Y. Yao, J. Li, L. Chen, H. Shi, M. Motta, C. Niu, U. Ray, S. Guo, R. J. Anderson, J. Li, L. N. Tran, C.-N. Yeh, B. Mussard, S. Sharma, F. Bruneval, M. van Schilfgaarde, G. H. Booth, G. K.-L. Chan, S. Zhang, E. Gull, D. Zgid, A. Millis, C. J. Umrigar, and L. K. Wagner (Simons Collaboration on the Many-Electron Problem), *Phys. Rev. X* **10**, 011041 (2020).
- ⁵⁴ C. A. Melton, M. C. Bennett, and L. Mitás, *The Journal of Chemical Physics* **144**, 244113 (2016), 1604.08876.
- ⁵⁵ C. A. Melton and L. Mitás, in *Recent Progress in Quantum Monte Carlo* (ACS Publications, 2016) pp. 1–13.
- ⁵⁶ C. A. Melton and L. Mitás, *Physical Review E* **96**, 043305 (2017), 1703.03481.
- ⁵⁷ C. A. Melton, M. C. Bennett, and L. Mitás, *Journal of Physics and Chemistry of Solids* **128**, 367 (2019).
- ⁵⁸ G. Ortiz, D. M. Ceperley, and R. M. Martin, *Phys. Rev. Lett.* **71**, 2777 (1993).
- ⁵⁹ F. D. Malone, S. Zhang, and M. A. Morales, *Journal of Chemical Theory and Computation* **15**, 256 (2019), 1810.00284.
- ⁶⁰ F. D. Malone, S. Zhang, and M. A. Morales, *Journal of Chemical Theory and Computation* **16**, 4286 (2020), 2003.09468.
- ⁶¹ W. Purwanto and S. Zhang, *Phys. Rev. E* **70**, 056702 (2004).
- ⁶² J. P. Perdew and Y. Wang, *Physical Review B* **45**, 13244 (1992).
- ⁶³ A. D. Becke, *The Journal of Chemical Physics* **98**, 1372 (1993), https://pubs.aip.org/aip/jcp/article-pdf/98/2/1372/11046762/1372_1.online.pdf.
- ⁶⁴ M. Holzmann, B. Bernu, V. Olevano, R. M. Martin, and D. M. Ceperley, *Phys. Rev. B* **79**, 041308(R) (2009).
- ⁶⁵ M. Holzmann, R. C. Clay, M. A. Morales, N. M. Tubman, D. M. Ceperley, and C. Pierleoni, *Phys. Rev. B* **94**, 035126 (2016).
- ⁶⁶ Y. Yang, N. Hiraoka, K. Matsuda, M. Holzmann, and D. M. Ceperley, *Phys. Rev. B* **101**, 165125 (2020).
- ⁶⁷ C. Lin, F. H. Zong, and D. M. Ceperley, *Phys. Rev. E* **64**, 016702 (2001).
- ⁶⁸ J. Kim, A. D. Baczewski, T. D. Beaudet, A. Benali, M. C. Bennett, M. A. Berrill, N. S. Blunt, E. J. L. Borda, M. Casula, D. M. Ceperley, S. Chiesa, B. K. Clark, R. C. Clay, K. T. Delaney, M. Dewing, K. P. Esler, H. Hao, O. Heinonen, P. R. C. Kent, J. T. Krogel, I. Kylänpää, Y. W. Li, M. G. Lopez, Y. Luo, F. D. Malone, R. M. Martin, A. Mathuriya, J. McMinis, C. A. Melton, L. Mitás, M. A. Morales, E. Neuscamman, W. D. Parker, S. D. Pineda Flores, N. A. Romero, B. M. Rubenstein, J. A. R. Shea, H. Shin, L. Shulenburger, A. F. Tillack, J. P. Townsend, N. M. Tubman, B. Van Der Goetz, J. E.

- Vincent, D. C. Yang, Y. Yang, S. Zhang, and L. Zhao, *Journal of Physics: Condensed Matter* **30**, 195901 (2018), 1802.06922.
- ⁶⁹ P. R. C. Kent, A. Annaberdiyev, A. Benali, M. C. Bennett, E. J. Landinez Borda, P. Doak, H. Hao, K. D. Jordan, J. T. Krogel, I. Kylänpää, J. Lee, Y. Luo, F. D. Malone, C. A. Melton, L. Mitas, M. A. Morales, E. Neuscammann, F. A. Reboredo, B. Rubenstein, K. Saritas, S. Upadhyay, G. Wang, S. Zhang, and L. Zhao, *The Journal of Chemical Physics* **152**, 174105 (2020), 2003.01831.
- ⁷⁰ P. Giannozzi, S. Baroni, N. Bonini, M. Calandra, R. Car, C. Cavazzoni, D. Ceresoli, G. L. Chiarotti, M. Cococcioni, I. Dabo, A. Dal Corso, S. de Gironcoli, S. Fabris, G. Fratesi, R. Gebauer, U. Gerstmann, C. Gougousis, A. Kokalj, M. Lazzeri, L. Martin-Samos, N. Marzari, F. Mauri, R. Mazzarello, S. Paolini, A. Pasquarello, L. Paulatto, C. Sbraccia, S. Scandolo, G. Sclauzero, A. P. Seitsonen, A. Smogunov, P. Umari, and R. M. Wentzcovitch, *Journal of Physics: Condensed Matter* **21**, 395502 (2009), 0906.2569.
- ⁷¹ P. Giannozzi, O. Andreussi, T. Brumme, O. Bunau, M. Buongiorno Nardelli, M. Calandra, R. Car, C. Cavazzoni, D. Ceresoli, M. Cococcioni, N. Colonna, I. Carnimeo, A. Dal Corso, S. de Gironcoli, P. Delugas, R. A. DiStasio, A. Ferretti, A. Floris, G. Fratesi, G. Fugallo, R. Gebauer, U. Gerstmann, F. Giustino, T. Gorni, J. Jia, M. Kawamura, H.-Y. Ko, A. Kokalj, E. Küçükbenli, M. Lazzeri, M. Marsili, N. Marzari, F. Mauri, N. L. Nguyen, H.-V. Nguyen, A. Otero-de-la Roza, L. Paulatto, S. Poncé, D. Rocca, R. Sabatini, B. Santra, M. Schlipf, A. P. Seitsonen, A. Smogunov, I. Timrov, T. Thonhauser, P. Umari, N. Vast, X. Wu, and S. Baroni, *Journal of Physics: Condensed Matter* **29**, 465901 (2017).
- ⁷² M. A. Marques, M. J. Oliveira, and T. Burnus, *Computer Physics Communications* **183**, 2272 (2012), 1203.1739.
- ⁷³ S. Lehtola, C. Steigemann, M. J. Oliveira, and M. A. Marques, *SoftwareX* **7**, 1 (2018).
- ⁷⁴ C. Attaccalite, S. Moroni, P. Gori-Giorgi, and G. B. Bachelet, *Physical Review Letters* **88**, 256601 (2002), 0109492 [cond-mat].
- ⁷⁵ N. D. Drummond and R. J. Needs, *Physical Review Letters* **102**, 126402 (2009).
- ⁷⁶ B. Bernu, L. Cândido, and D. M. Ceperley, *Physical Review Letters* **86**, 870 (2001).
- ⁷⁷ S. Chiesa, D. M. Ceperley, R. M. Martin, and M. Holzmann, *Phys. Rev. Lett.* **97**, 076404 (2006).

I. SUPPLEMENTARY MATERIAL

Figure 5 shows FP-DMC, HF, and DFT charge densities before and after the metal-insulator transition (MIT) at $r_s = 3$. Hybrid LDA is the only density functional that reasonably reproduces QMC charge density on both sides of the MIT. In Fig. 6, we show the evolution of charge density across the MIT. Only hybrid LDA and QMC have a discontinuous jump across the transition.

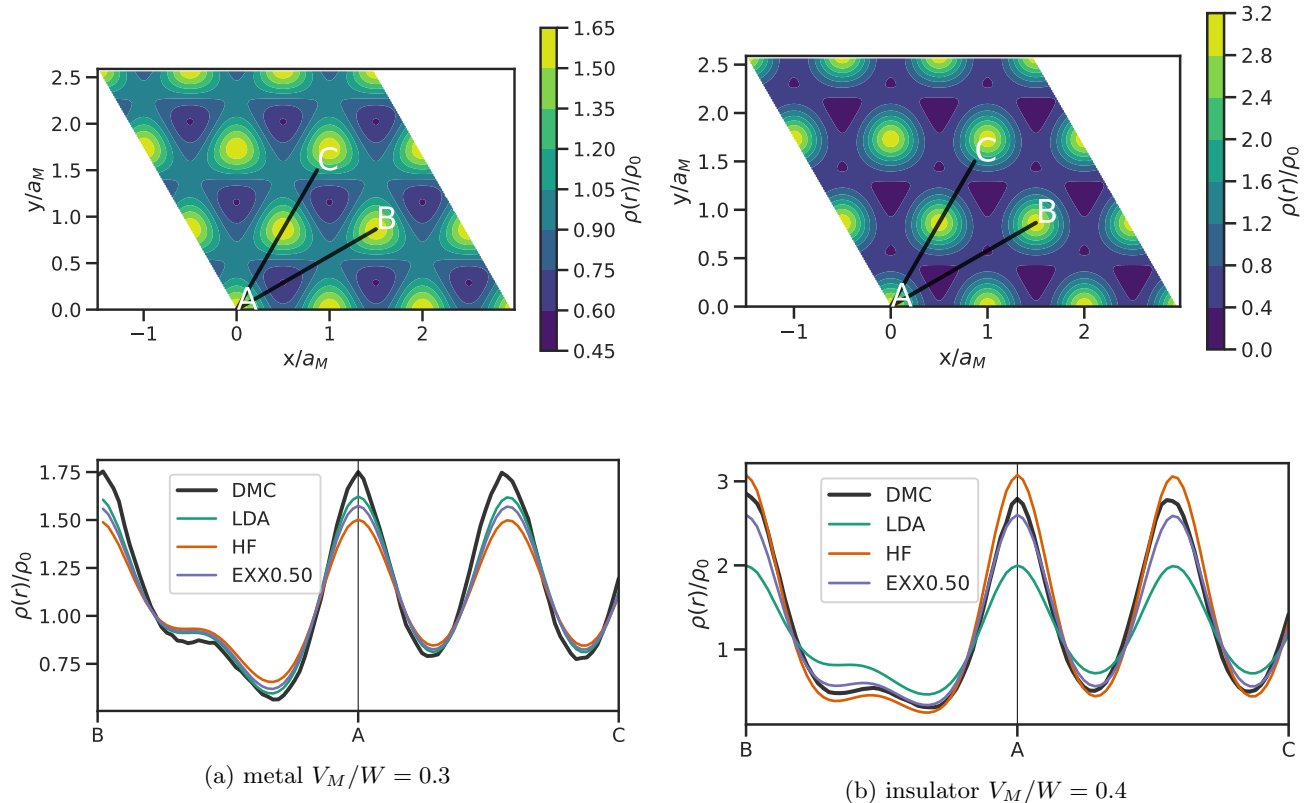


FIG. 5. FP-DMC ($N=144$) charge density at $r_s = 3$ along the linecut BAC. Charge densities from three effective one-body theories are shown along with the QMC linecuts. All functionals produce reasonable charge density for the metallic phase, but only hybrid LDA agrees well with QMC in the insulating phase.

Table I lists the FP-DMC energy for the calculations shown in Fig. 5. At each point on the phase diagram, we compute two FP-DMC energies using Slater-Jastrow trial wavefunctions built from HF and LDA orbitals. We choose the lowest-energy trial to calculate QMC properties. The LDA trial changes from a magnetic insulator to a magnetic metal (spin density wave phase) then to a non-magnetic metal. The HF trial is magnetic and insulating and its FP-DMC energy becomes higher than that of the LDA trial in only the non-magnetic metal phase.

TABLE I. Twist averaged FP-DMC energies in Hartree at $r_s = 3$.

(a) metallic phase					(b) insulating phase						
mag	r_s	V_M/W	N	func	E/N	mag	r_s	V_M/W	N	func	E/N
120	3.0	0.3	144	HF	-0.21824(6)	120	3.0	0.4	144	HF	-0.23262(4)
120	3.0	0.3	144	LDA	-0.22130(1)	120	3.0	0.4	144	LDA	-0.23003(2)
para	3.0	0.3	144	HF	-0.22121(1)	para	3.0	0.4	144	HF	-0.23022(2)
para	3.0	0.3	144	LDA	-0.22129(1)	para	3.0	0.4	144	LDA	-0.23037(2)
stripe	3.0	0.3	144	HF	-0.21828(5)	stripe	3.0	0.4	144	HF	-0.23240(4)
stripe	3.0	0.3	144	LDA	-0.22128(1)	stripe	3.0	0.4	144	LDA	-0.23039(2)

Figure 7 shows a comparison of FP-DMC and ph-AFQMC magnetization densities of the 120° Néel phase at $r_s = 3$ and $\lambda = 0.6$. Both calculations averaged over 16 twists, each containing 36 electrons. On average, 140 HF orbitals at

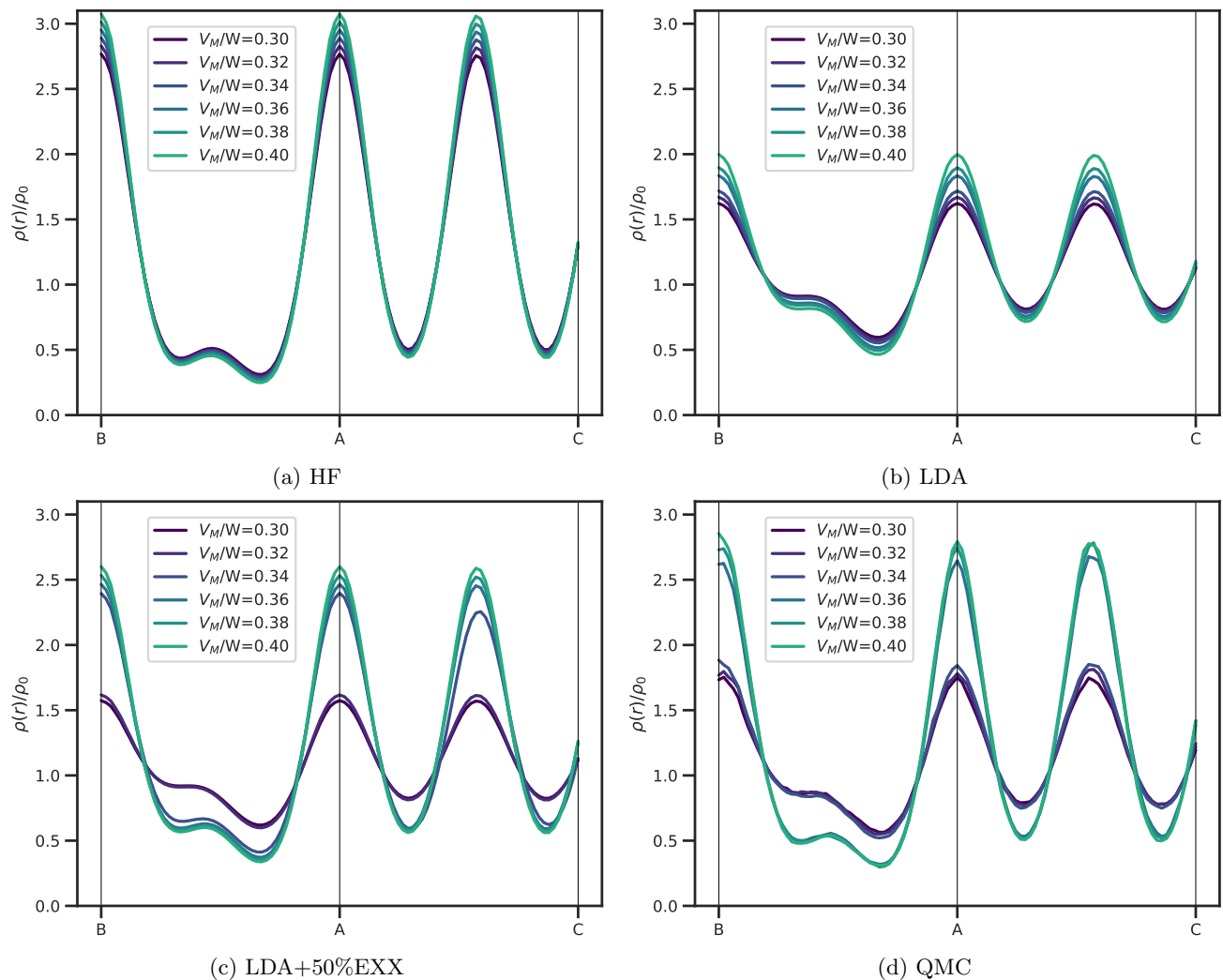


FIG. 6. Charge density linecuts (same as Fig. 5) across the metal insulator transition at $r_s = 3$.

each twist were used as basis functions in AFQMC. The DMC calculation of the same system used a Slater-Jastrow trial wavefunction built from the occupied HF orbitals. Densities from the two methods are consistent despite the very different approximations in the algorithms.

To make an order-of-magnitude estimate for the magnetic ordering temperature, we calculate the energy cost of a single spin flip ΔE and related it to the exchange parameter $J = \Delta E/4$ in a nearest-neighbor Heisenberg model of the spin stripe phase. We made the estimates at $r_s = 8$ using a 36-electron system and FP-DMC with Slater-Jastrow wavefunction and LDA orbitals. As shown in Fig. 8, J decreases rapidly from $O(100)$ mK at $\lambda = 0.4$ to within errorbars of zero at $\lambda = 1.6$. Given the deep moiré potential measured in experiments⁵, we do not expect the ground-state magnetic order to be measurable because of large thermal fluctuations.

Figure 9 shows finite-size correction (FSC)^{65,77} and thermodynamic extrapolation⁷⁵ at $r_s = 3$ and $\lambda = 0.3, 0.4$. The two approaches agree in simulation cells containing 144 electrons in both the metallic and the insulating phases. To calculate the FSC, we fit the fluctuating structure factor $\delta S(k) = \langle (\rho_{\mathbf{k}} - \langle \rho_{\mathbf{k}} \rangle)(\rho_{-\mathbf{k}} - \langle \rho_{-\mathbf{k}} \rangle) \rangle$ to $ak^{3/2} + bk^2 + ck^4$ as shown in Fig. 10. The potential energy correction is calculated as $\delta V = [\int - \sum] \frac{1}{2} v_{\mathbf{k}} \delta S(k)$, while the kinetic energy correction is approximated to leading-order $\delta T \approx \delta V$. These results show that the 144-electron system is large enough to accurately estimate the total energy in the thermodynamic limit.

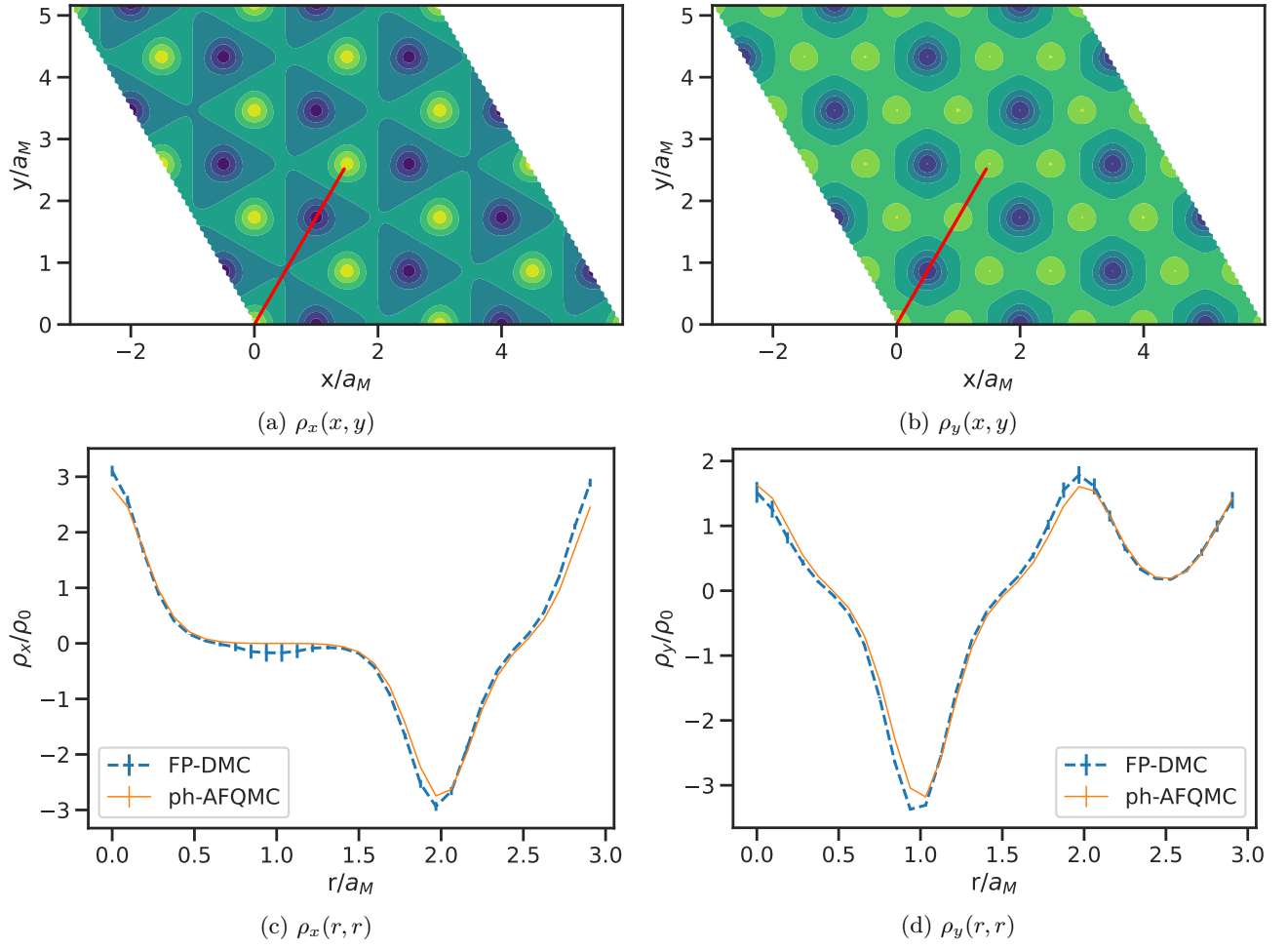


FIG. 7. Magnetization density of AFQMC and DMC at $r_s = 3$ and $\lambda = 0.6$.

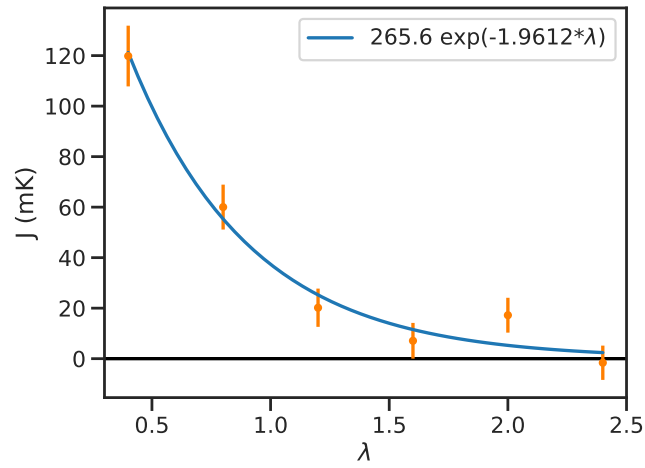


FIG. 8. Estimates of the exchange parameter J of a nearest-neighbor Heisenberg model at $r_s = 8$.

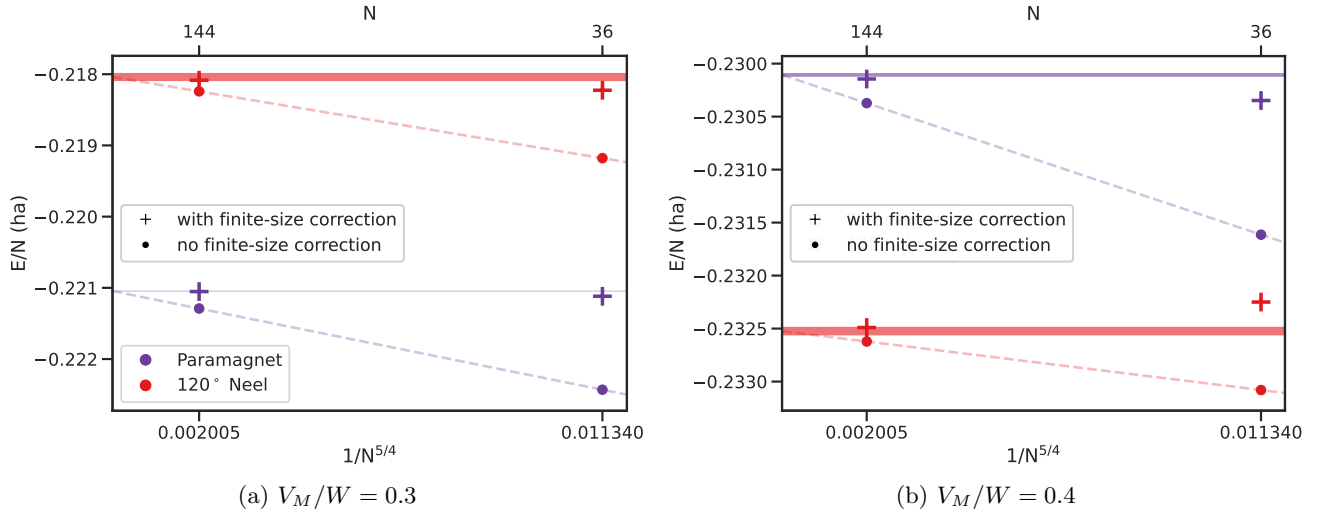


FIG. 9. Finite-size correction (FSC) and extrapolation of FP-DMC total energy at $r_s = 3$. The faint dashed line shows size extrapolation. The horizontal line and its width represent the mean and error of the thermodynamic limit. It agrees with $N = 144$ result with FSC.

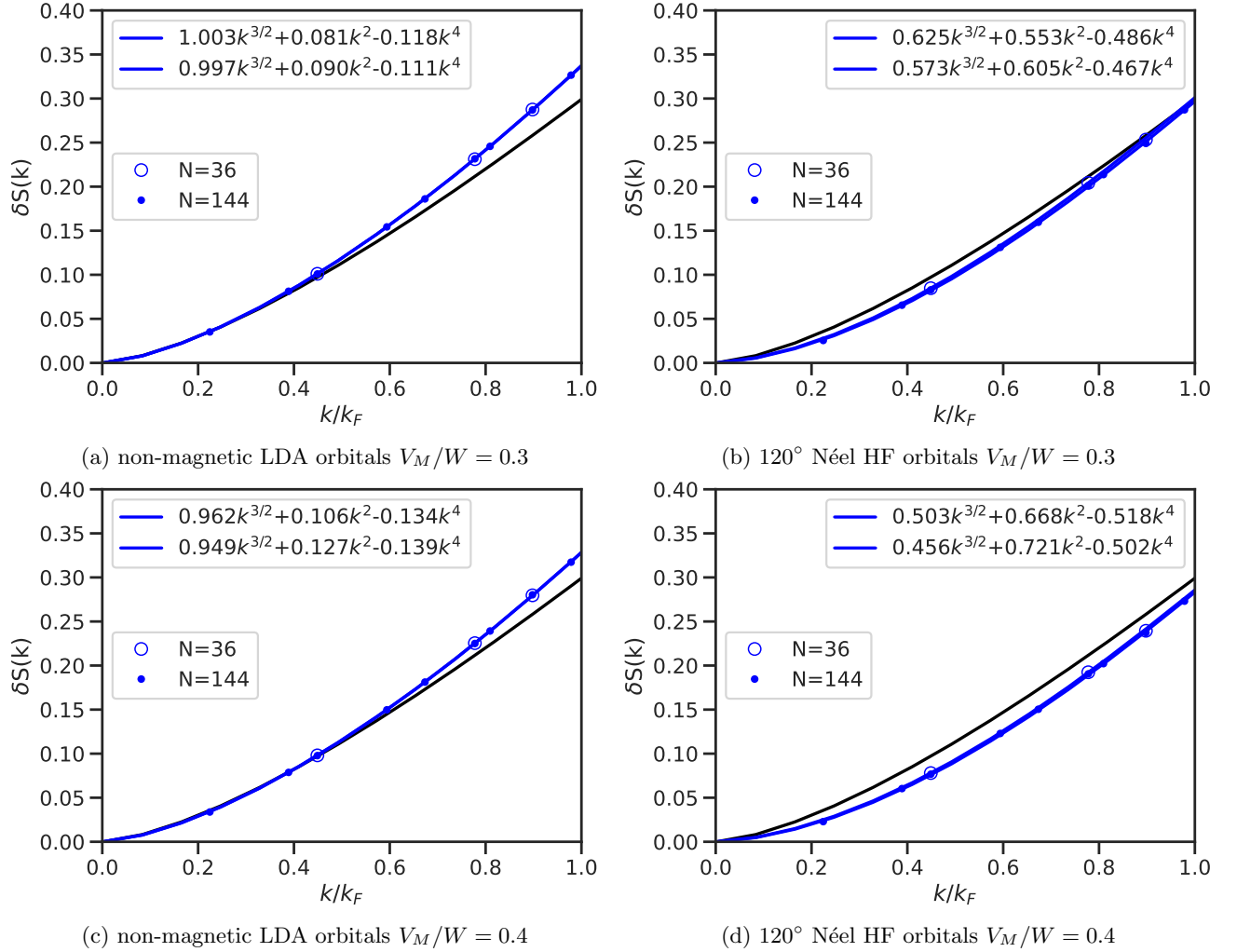


FIG. 10. Fluctuating structure factor $\delta S(k)$ at $r_s = 3$. The black solid line is reference from random phase approximation (RPA), which exactly captures the long-wavelength plasmon fluctuations in the metallic phase. Blue lines are polynomial fits to the FP-DMC data.